Rock Mechanics and Rock Engineering
https://doi.org/10.1007/s00603-024-03763-3

ORIGINAL PAPER

Combination of a Failure Index and a Dilatancy-Dependent Permeability Model in Hydro-Mechanically-Coupled Numerical Simulations of Argillaceous Rock Formations of the Callovo-Oxfordian (COx)

Eike Radeisen[1,2] · Hua Shao[1] · Michael Pitz[1,3] · Jürgen Hesser[1] · Olaf Kolditz[2,4] · Wenqing Wang[4]

Received: 4 January 2023 / Accepted: 5 January 2024

Abstract

Hydraulic-mechanical coupling in claystone is of great importance for repository research, as claystone is considered a possible host rock and hydraulic-mechanical coupled processes can affect the integrity of the barrier. Of particular importance in this context are excavation damage zones and hydraulically-induced microcracks and fractures. In this work, two constitutive equations developed for these hydraulic-mechanical coupled processes are combined in a novel way. The approach exploits the different dominant stress states that prevail in the respective processes. This approach is applied in several numerical simulations for validation and compared with experimental data. The measured data were obtained during gas-injection tests in the scope of the PGZ experiment in the underground laboratory of Bure, France, where the hydraulic-mechanical coupling of the is the Nabla operator claystone was investigated. Five numerical models were calculated, each with a different model configuration, to simulate the excavation damage zone and dilatancy-controlled flow during gas-injection tests. The numerical results show that the developed approach can first satisfactorily predict the extent and behaviour of the excavation damage zone under different stress conditions and the subsequent dilatancy-dependent permeability due to the increased gas pressure.

Highlights

- Novel approach to combine two constitutive material models to better numerically simulate microcracks in argillaceous rocks.
- Comparison of different model configurations to show the effect of the approach and to enable calibration of the dilatancy-controlled model.
- The combination of excavation damage zone and dilatancy-controlled permeability allows short-term gas pressures to be reproduced well.

Keywords H^2M coupling · Gas migration · Failure index permeability · Dilatancy-controlled flow · OpenGeoSys

✉ Eike Radeisen
eike.radeisen@bgr.de

[1] Federal Institute for Geosciences and Natural Resources (BGR), 30655 Hannover, Germany

[2] Technische Universität Dresden, 01069 Dresden, Germany

[3] Technische Universität Bergakademie Freiberg, 09599 Freiberg, Germany

[4] Helmholtz Center for Environmental Research (UFZ), 04341 Leipzig, Germany

List of symbols

Greek symbols

α	Biot coefficient
$\varepsilon_{\mathrm{vol}}$	Volumetric strain
$\boldsymbol{\varepsilon}_{\mathrm{t}}$	Total strain
$\boldsymbol{\varepsilon}_{\mathrm{el}}$	Elastic strain
$\boldsymbol{\varepsilon}_{\mathrm{pl}}$	Plastic strain
η_{ξ}	Viscosity of the phase ξ
$\boldsymbol{\nu}$	Poisson ‘s ratio

Published online: 15 April 2024

ξ	Fluid phases (w: wetting fluid, g: non-wetting fluid)
ρ	Bulk density
ρ_ξ	Density of the phase ξ
ρ_s	Density of solid grains
$\boldsymbol{\sigma}$'	Effective stress
$\boldsymbol{\sigma}$	Total stress
σ_1	Major principal stresses
σ_3	Minor principal stresses
σ_m	Mean stress
σ_t	Tensile strength
T	Tortuosity
τ_f	Shear strength
τ_m	Maximum shear stress
ϕ	Porosity
φ	Inner friction angle

Roman symbols

B	Fitting parameter failure index
b_1,b_2, b_3	Fitting parameter strain-dependent permeability
c	Cohesive strength
E	Oung's modulus
f	Failure-index function
f_{sdp}	Strain-dependent permeability function
$\mathbf{G}$	Shear modulus
$\mathbf{g}$	Gravitational acceleration
H	Heaviside step function
$\mathbf{I}$	Identity tensor
$\mathbf{k}$	Intrinsic permeability
$\mathbf{k}_0$	Initial intrinsic permeability
k_r	Reference permeability
k^r_ξ	Relative permeability of the phase ξ
M^{H2O}	Water molar mass
M^{N2}	Nitrogen molar mass
n	Van Genuchten material parameter
p_c	Capillary pressure (suction)
p_{entry}	Gas entry pressure
p_p	Pore pressure
p_ξ	Pressure of the phase ξ
Q_ξ	Source and sink term of the phase ξ
S_{max}	Maximum saturation of the wetting fluid
S_r	Residual saturation of the wetting fluid
S_ξ	Saturation of the phase ξ

Operators

∇	Nabla operator
$\dot{(\bullet)}$	Temporal derivative of $(\bullet)$

1 Introduction

The characterisation of gas transport through claystone is of great importance for the safety assessment of a repository for radioactive materials, as claystone is considered a possible host rock for such a repository (de La Vaissière et al. 2015). In conventional continuum models, multiphase flow in porous media is often modelled with standard two-phase flow models. However, in addition to standard two-phase flow, complex hydraulic-mechanical coupled constitutive equations are necessary to describe gas flow in claystone, as these can better represent the observed processes (Seyedi et al. 2021). Gas flow in claystone during in-situ investigations with high-gas pressures is dependent on an EDZ, dilatancy-induced permeability alteration and hydraulic fracturing of the rock (de La Vaissière et al. 2015). In continuum mechanics, there are numerous well-established empirical solutions for those processes, although no general theory or concept can describe all processes related to gas transport through claystone.

Approaches to numerically simulate the EDZ have been developed by Jung et al. (2023), Manica et al. (2017), Pardoen and Collin (2017), Souley et al. (2017), Vu et al. (2020) and Wang et al. (2021), among others. The developed approaches employ sophisticated hydro-mechanical models with strength hardening and softening (Manica et al. 2017), strain localisation (Pardoen and Collin 2017; Vu et al. 2020), elasto-viscoplasticity (Manica et al. 2017; Souley et al. 2017) and damage (Manica et al. 2017; Souley et al. 2017; Wang et al. 2021). Empirical or semi-empirical hydro-mechanical (HM) coupled models developed in the framework of Biot's consolidation theory simulating dilatancy-controlled gas flow have also been proposed by several authors (Gerard et al 2014; Nguyen and Le, 2015; Olivella and Alonso 2008; Radeisen et al. 2023a; Senger et al 2014; Senger et al 2018; Xu et al 2013; Yang et al 2020).

In this paper, two constitutive sets of equations are combined, which are used to model gas flow in the EDZ and the dilatancy-dependent gas flow. The two constitutive equation sets are based on different dominant failure modes, the shear failure mode during excavation and the tensile failure mode during gas-injection testing. The developed approach is applied in a numerical simulation of the PGZ experiment at the Meuse/Haute-Marne Underground Research Laboratory (MHM URL) in France (Delay et al. 2011). The PGZ experiment was conducted by the French National Radioactive Waste Management Agency (ANDRA) to investigate the effects of stress alignment and permeability increase induced by drilling/excavation and the effect of gas injection on the barrier integrity of the Callovo-Oxfordian (COx) argillaceous rock formation (Plúa et al. 2021). The simulated-gas-injection test was carried out in December 2020 in boreholes PGZ1002 and PGZ1003, which are aligned parallel to the minor and major horizontal stress, respectively. The COx is a well-examined and characterised argillaceous rock formation, so that the values of the material parameters can be well determined and the results can be validated more accurately (Belmokhtar et al. 2016; Plúa et al. 2021; Seyedi et al. 2017).

In-situ measurements are available for the COx with regard to the dimension and characteristics of the EDZ (Armand et al. 2014; de La Vaissière et al. 2015). Measurements of the gas pressure and water pressure in the injection filter are available for the gas-injection test in PGZ1003, provided by the DECOVALEX-2023 project (Birkholzer and Bond 2022) and used for a comparison with the numerical results.

The numerical application is conducted with the open-source code OpenGeoSys (OGS). OGS is based on an object-oriented finite element method (FEM) and has been developed since the mid-1980s as an open-source initiative for numerical simulations of thermo-hydro-mechano-chemical processes in porous and fractured media (Kolditz et al. 2012). Similiar hydro-mechanically coupled simulations were performed in recent years with the numerical code on bentonites (Radeisen et al. 2023b, Radeisen et al. 2024). The paper first presents the numerical fundamentals including balance equations and the approach for combining the permeability constitutive models. Subsequently, the experiment is presented and the phases of the simulation are described. Finally, the results are presented and a short conclusion is given.

2 Numerical Methods

2.1 Balance Equations

The two-phase hydraulic-mechanical (H^2M) coupled processes are calculated by a staggered scheme. The processes are based on the balance equations. The coupled processes satisfy the following equations at all times. The momentum balance equation, derived from the effective stress law can be expressed as follows (Wang et al. 2011):

$$\nabla \cdot \left[\boldsymbol{\sigma}' - \alpha\left(p_\mathrm{g} - S_\mathrm{w} p_\mathrm{c}\right)\mathbf{I}\right] + \rho\mathbf{g} = 0 \tag{1}$$

where ∇ is the Nabla operator, $\boldsymbol{\sigma}'$ is the effective stress, α is the Biot coefficient, p_g is the pressure of the gaseous phase (non-wetting phase), S_w is the saturation of the wetting fluid, p_c is the capillary pressure (suction), $\mathbf{I}$ is the identity tensor, ρ is the bulk density and $\mathbf{g}$ is the gravitational acceleration. The wetting fluid is assumed to behave as an immiscible Newtonian fluid. Since phase transitions and dissolutions are of little significance in simulations with high-gas injection rates, phase immiscibility is adopted as a simplification here. Assuming an isothermal two-phase flow process, the balance equation for the wetting phase can be expressed as follows:

$$\phi\rho_\mathrm{w}\frac{\partial S_\mathrm{w}}{\partial p_\mathrm{c}}\dot{p}_\mathrm{c} + \alpha\rho_\mathrm{w}S_\mathrm{w}\nabla\cdot\dot{\mathbf{u}} + \nabla\cdot\left[\rho_\mathrm{w}\frac{\mathbf{k}k^\mathrm{r}_\mathrm{w}}{\eta_\mathrm{w}}\left(-\nabla p_\mathrm{g} + \nabla p_\mathrm{c} + \rho_\mathrm{w}\mathbf{g}\right)\right] = Q_\mathrm{w} \tag{2}$$

where ϕ is the porosity, ρ_w is the density of the wetting fluid, $\dot{p}_\mathrm{c} = \mathrm{d}p_c/\mathrm{d}t$ is the temporal derivative of the capillary pressure, $\dot{\mathbf{u}} = \mathrm{d}\mathbf{u}/\mathrm{d}t$ is the temporal derivative of the solid displacement vector, $\mathbf{k}$ is the intrinsic permeability, k^r_w is the relative permeability of the wetting fluid, η_w is the viscosity of the wetting fluid and Q_w represents the source and sink term of the wetting fluid. Similarly, the mass balance equation of the gas phase can be expressed as follows:

$$-\phi\rho_\mathrm{g}\frac{\partial S_\mathrm{w}}{\partial p_\mathrm{c}}\dot{p}_\mathrm{c} + \alpha\rho_\mathrm{g}(1-S_\mathrm{w})\nabla\cdot\dot{\mathbf{u}} + \phi(1-S_\mathrm{w})\left(\frac{\partial\rho_\mathrm{g}}{\partial p_\mathrm{g}}\dot{p}_\mathrm{g} + \frac{\partial\rho_\mathrm{g}}{\partial p_\mathrm{c}}\dot{p}_\mathrm{c}\right) + \nabla\cdot\left[\rho_\mathrm{g}\frac{\mathbf{k}k^\mathrm{r}_\mathrm{g}}{\eta_\mathrm{g}}\left(-\nabla p_\mathrm{g} + \rho_\mathrm{g}\mathbf{g}\right)\right] = Q_\mathrm{g} \tag{3}$$

where ρ_g is the density of the non-wetting fluid,$\dot{p}_\mathrm{g} = \mathrm{d}p_g/\mathrm{d}t$ is the temporal derivative of the non-wetting fluid pressure, k^r_g is the relative permeability of the non-wetting fluid, η_g is the viscosity of the non-wetting fluid and Q_g represents the source and sink term of the non-wetting fluid. All balance equations are formulated with the primary variables $\mathbf{u}$, p_g and p_c as implemented in the H^2M process in OGS. Detailed derivations of the balance equations can be found in (Kolditz et al. 2012).

2.2 Hydraulic Constitutive Equations

In the H2M process of OGS, the capillary pressure and the phase pressure of the non-wetting fluid are primary variables. The pressure of the liquid phase is consequently defined as:

$$p_\mathrm{w} = p_\mathrm{g} - p_\mathrm{c} \tag{4}$$

Equation (4) can be used to calculate the pore pressure (p_p), based on $S_\mathrm{w} + S_\mathrm{g} = 1$ as:

$$p_\mathrm{p} = S_\mathrm{g}p_\mathrm{g} + S_\mathrm{w}p_\mathrm{w} = p_\mathrm{g} - S_\mathrm{w}p_\mathrm{c} \tag{5}$$

The saturation can be calculated with the van Genuchten equation (van Genuchten 1980):

$$S_\mathrm{w} = \begin{cases} \left(\left(\frac{p_\mathrm{c}}{p_\mathrm{entry}}\right)^\mathrm{n}\right)^{\frac{1-n}{n}}, & p_\mathrm{c} > 0 \\ 1, & p_\mathrm{c} \le 0 \end{cases} \tag{6}$$

where p_entry is the gas entry pressure and n is an empirical material parameter. However, since the porous medium exhibits some residual saturation and a maximum saturation at all times, the effective saturation of the wetting liquid S_e is calculated as follows:

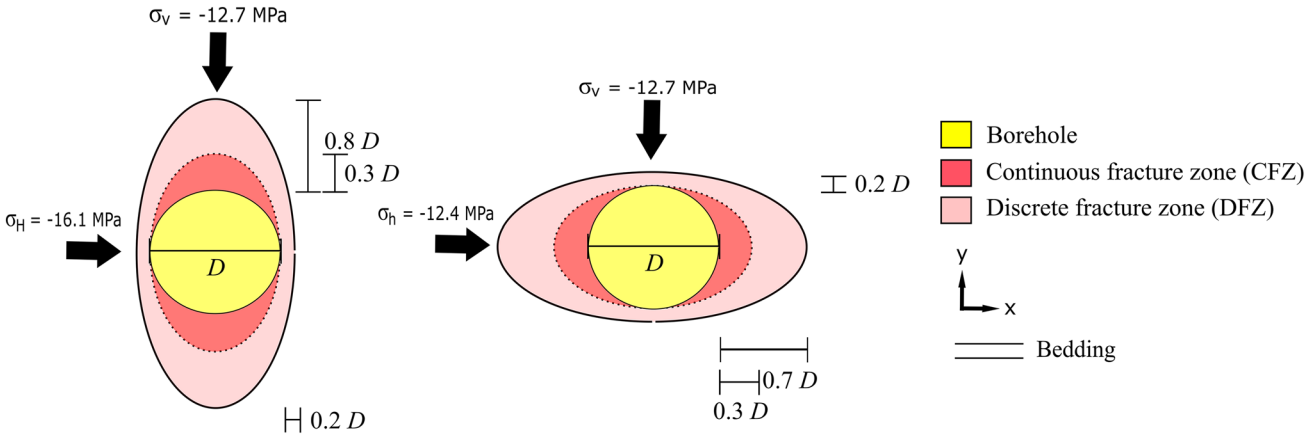

Fig. 1 Schematic representation of the excavation damage zone with measured values from Armand et al. (2014)

$$S_e = \frac{S_w - S_r}{S_{max} - S_r} \tag{7}$$

where S_r is the residual saturation of the wetting fluid and S_{max} is the maximum saturation of the wetting fluid. The relative permeability in the porous medium of the two fluid phases depends on the effective saturation. The relative permeability for the wetting fluid is according to the Mualem analytical function (Mualem 1976) as follows:

$$k_w^r = S_e^{\frac{1}{2}} \left[1 - \left(S_e^{\frac{n}{n-1}} \right)^{\left(1-\frac{1}{n}\right)} \right]^2 \tag{8}$$

The relative permeability of the non-wetting liquid is described with a cubic function, which is represented as follows:

$$k_g^r = 100\left(1 - S_w\right)^3 \tag{9}$$

The cubic function is multiplied by a factor of 100 to account for measurements that the intrinsic permeability in the COx is about 100 times higher for the non-wetting fluid than for the wetting fluid (Amri et al. 2022; Zhang and Rothfuchs 2004).

The Darcy law (Darcy 1856) calculates the flow of both fluid phases (**q**) based on the relative permeabilities and fluid pressures as follows:

$$\mathbf{q}_\xi = -\rho_\xi \frac{\mathbf{k} k_\xi^r}{\eta_\xi} \left(\nabla p_\xi - \rho_\xi \mathbf{g} \right) \tag{10}$$

where the subscript ξ stands for both fluid phases (w: wetting fluid, g: non-wetting fluid).

Table 1 Application areas in the mechanical stress state of the constitutive equation sets and their effects on the permeability

Mechanical stress state	Compression		Tension
Failure	Shear failure	No failure	Tensile failure
Permeability model	Failure-index permeability	Dilatancy-induced permeability	
Effect	Increasing **k**	Decreasing **k**	Increasing **k**

2.3 Mechanically-Coupled Permeability Constitutive Equations

After drilling the boreholes, two zones can be identified in the resulting EDZ: a continuous fracture zone (CFZ) with extensional and shear fractures and a discrete fracture zone (DFZ) with only shear fractures (Armand et al. 2014). The CFZ is located around the borehole, while the DFZ is generally more extensive. The overall BDZ is likely to have an ellipsoidal shape, and its structure depends on the orientation of the borehole axis with respect to the principal stresses and bedding (Armand et al. 2013, 2014). A schematic representation of the EDZ with division into CFZ and DFZ can be seen in Fig. 1.

In this work, the H2M-coupled behaviour in the COx during excavation and under a high-gas-injection rate is simulated by two constitutive equation sets. The combination of the two equation sets is based on the different fracture modes of the investigated processes (Table 1). The excavation-induced permeability increase in the vicinity of the borehole is assumed to be triggered by unloading tensile fractures (mode I) and shear fractures due to stress redistribution (Armand et al. 2013). In this work it is assumed that the dimension of the EDZ is equal to the dimension of the DFZ and is determined by shear

fractures. Tensile fractures in the CFZ region are implicitly represented by high permeability values near the borehole. In the case of a shear-stress induced yield, the permeability variation is determined by the failure-index permeability model (Wang et al. 2021). During the subsequent gas injection, diffusion and conventional two-phase flow initially occur in a negligible proportion (Senger et al. 2018). Should the gas pressure increase to a point where it corresponds approximately to the minor principal stress, dilatancy-controlled gas propagation occurs in the claystone and the permeability will increase. Dilatancy is defined in this context as inelastic volumetric change of the rock. This process is associated with a local volume reduction in the case of compressive stresses or with pathway dilation in the case of tensile stresses (Horseman 1996). The numerical implementation of this process is carried out with the strain-dependent permeability model (Xu et al. 2013).

To prevent the two constitutive sets of equations from overlapping and multiplying each other in the area of the shear failure (during excavation), the respective sets are only activated in the corresponding stress states. To implement this numerically, the failure index f is calculated for the shear failure (Wang et al. 2021):

$$f = \frac{|\tau_{\mathrm{m}}|}{\cos(\varphi)\tau_f(\sigma_{\mathrm{m}})} \tag{11}$$

where $\tau_{\mathrm{m}} = (\sigma_1 - \sigma_3)/2$ is the maximum shear stress, calculated with the major and minor principal stresses σ_1 and σ_3, φ is the inner friction angle and $\tau_f(\sigma_{\mathrm{m}})$ is the shear strength dependent on the mean stress $\sigma_{\mathrm{m}} = (\sigma_1 + \sigma_3)/2$. The shear strength is calculated by the Mohr–Coulomb failure criterion (Labuz & Zang 2012):

$$\tau_{\mathrm{f}}(\sigma_{\mathrm{m}}) = c - \sigma_{\mathrm{m}}\tan(\varphi) \tag{12}$$

where c is the cohesion. The Mohr–Coulomb equation is used here as the failure criterion, since the failure-index model is formulated on its basis, even though it is only a rough approximation of the yield strength and other failure criteria such as Drucker-Prager (Chiarelli et al. 2003) or Hoek–Brown (Souley et al. 2017) provide a better approximation of the yield strength in COx. The constitutive set of equations is determined using the failure index, whereby the following applies:

$$\text{constitutive equation} = \begin{cases} \textit{failure index dependent permeability} & \text{if } f \geq 1 \\ \textit{dilatancy induced permeability} & \text{if } f < 1 \end{cases} \tag{13}$$

2.3.1 Failure Index-Dependent Permeability

The failure index-dependent permeability model was developed by Wang et al. (2021) and is implemented in OGS-5.

$$\mathbf{k} = \mathbf{k}_0 + H(f-1)k_{\mathrm{r}}e^{bf}\mathbf{I} \tag{14}$$

where $\mathbf{k}_0$ is the initial intrinsic permeability, H is the Heaviside step function, k_{r} is a reference permeability, b is a fitting parameter. The model is originally defined for both shear and tensile fractures, but is only applied here for shear fractures. Since shear fractures from the drilling process affect a larger area, this assumption is made for simplification, even though it does not completely correspond to the observed in-situ processes. The failure index f used in the permeability model was defined in Eq. (11) and can be calculated with the Mohr–Coulomb failure criterion Eq. (12). Wang et al. (2021) have previously calibrated the empirical values of the equation on COx claystone.

2.3.2 Dilatancy-Induced Permeability

The permeability increase in the process of dilatant deformations is simulated in the model by the strain-dependent permeability model, developed by Xu et al. (2013). This is a hydraulic-mechanical-coupled empirical model based on volumetric strain and equivalent plastic strain. The parameters are supplemented with empirical values depending on the prevailing stress state. As a result, permeability decreases in the compressed stress state and increases in the extensional stress state. These functions are regulated by the volumetric deformation (Braun et al. 2020). The equivalent plastic deformation may exclusively contribute to an exponential increase in permeability.

$$\mathbf{k} = f_{sdp}(\varepsilon_{\mathrm{vol}})e^{b_1\bar{\varepsilon}_{\mathrm{pl}}}\mathbf{k}_0 \tag{15}$$

where $\varepsilon_{\mathrm{vol}}$ is the volumetric strain, b_1 is an empirical value related with the permeability increase due to tensile plastic deformation, $\bar{\varepsilon}_{\mathrm{pl}}$ is the equivalent plastic strain. The function f_{sdp} is dependent on the behaviour of the volumetric strain as follows:

$$f_{sdp}(\varepsilon_{\mathrm{vol}}) = \begin{cases} 10^{b_2\varepsilon_{\mathrm{vol}}}, & \varepsilon_{\mathrm{vol}} \leq 0 \text{ (compaction)} \\ 10^{b_3\varepsilon_{\mathrm{vol}}}, & \varepsilon_{\mathrm{vol}} > 0 \text{ (extension)} \end{cases} \tag{16}$$

where b_2 and b_3 are empirical values related to the decrease and increase of the permeability due to dilatancy,

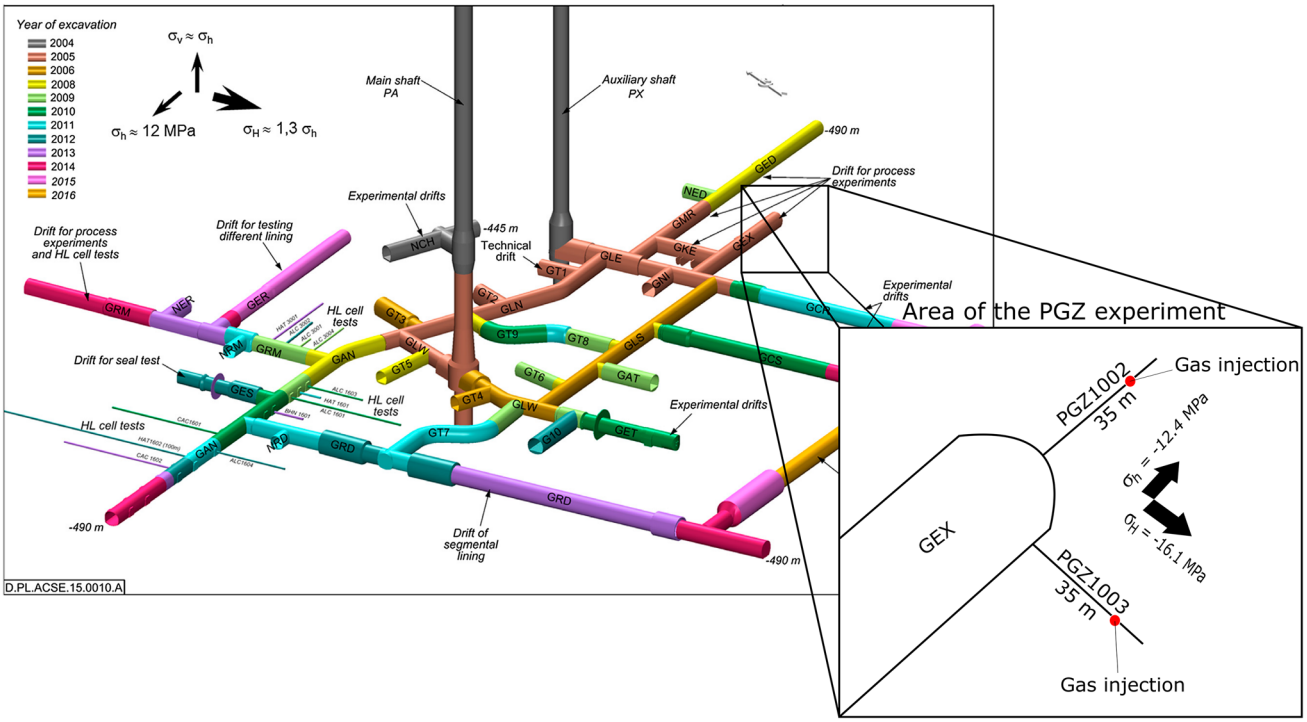

Fig. 2 Layout of the MHM URL with the area highlighted where the PGZ experiment was carried out (edited after Seyedi et al. 2017)

respectively. To account for microfractures due to tensile forces, a tension cut-off is added to the yield criterion. The tension cut-off is directly related to the equivalent plastic strain and is formulated based on Eq. (12). A description of the non-associated yield criterion and the implementation to OGS can be found in Nagel et al. (2017).

2.4 Mechanical Constitutive Equations

The mechanical regime is based on elasto-plasticity for the COx as previously shown in Eqs. (11) and (12), to account for permeability caused by failure or plastic dilatancy. The elastic behaviour of the COx is orthotropic. The stress state can be calculated using the effective stress law, noting that the tensile stress is defined as positive, as follows:

$$\boldsymbol{\sigma} = \boldsymbol{\sigma}\prime - \alpha p_{\mathrm{p}}\mathbf{I} \tag{17}$$

where $\boldsymbol{\sigma}$ is the total stress. The effective stress can be used to calculate the elastic strain, by using the Hooke's law, which can be expressed in a generalized form as follows:

$$\boldsymbol{\sigma} = \mathbf{C}\boldsymbol{\varepsilon} \tag{18}$$

where $\mathbf{C}$ is the stiffness tensor and $\boldsymbol{\varepsilon}$ is the strain tensor. Since plane strain conditions apply in the simulated models ($\varepsilon_{zz} = \varepsilon_{zx} = \varepsilon_{yz} = 0$), Hooke's law for an orthotropic material can be expressed as follows:

$$\begin{bmatrix} \varepsilon_{xx} \\ \varepsilon_{yy} \\ 2\varepsilon_{xy} \end{bmatrix} = \begin{bmatrix} \frac{1-\nu_{xy}\nu_{yx}}{E_x} & -\frac{\nu_{yx}-\nu_{xy}\nu_{yx}}{E_y} & 0 \\ -\frac{\nu_{xy}-\nu_{xy}\nu_{yx}}{E_x} & \frac{1-\nu_{xy}\nu_{yx}}{E_y} & 0 \\ 0 & 0 & \frac{1}{G_{xy}} \end{bmatrix} \begin{bmatrix} \sigma_{xx} \\ \sigma_{yy} \\ \tau_{xy} \end{bmatrix} \tag{19}$$

where $\boldsymbol{\nu}$ is the Poisson's ratio and $\mathbf{G}$ is the shear modulus. The strain can be divided into elastic and plastic strain as follows:

$$\boldsymbol{\varepsilon}_{\mathrm{t}} = \boldsymbol{\varepsilon}_{\mathrm{el}} + \boldsymbol{\varepsilon}_{\mathrm{pl}} \tag{20}$$

where $\boldsymbol{\varepsilon}_{\mathrm{t}}$ is the total strain, $\boldsymbol{\varepsilon}_{\mathrm{el}}$ is the elastic strain and $\boldsymbol{\varepsilon}_{\mathrm{pl}}$ is the plastic strain.

3 Modelling the PGZ Experiment

3.1 PGZ Experiment

The PGZ experiment was conducted in the Meuse/Haute-Marne Underground Research Laboratory (MHM URL), France (Fig. 2). The MHM URL has been in operation since 2000. All relevant aspects of the final disposal of radioactive materials in the connection with argillaceous rocks are investigated there (Plúa et al. 2021). Among other experiments, the PGZ experiment was carried out by ANDRA at the MHM URL to investigate gas flow processes through

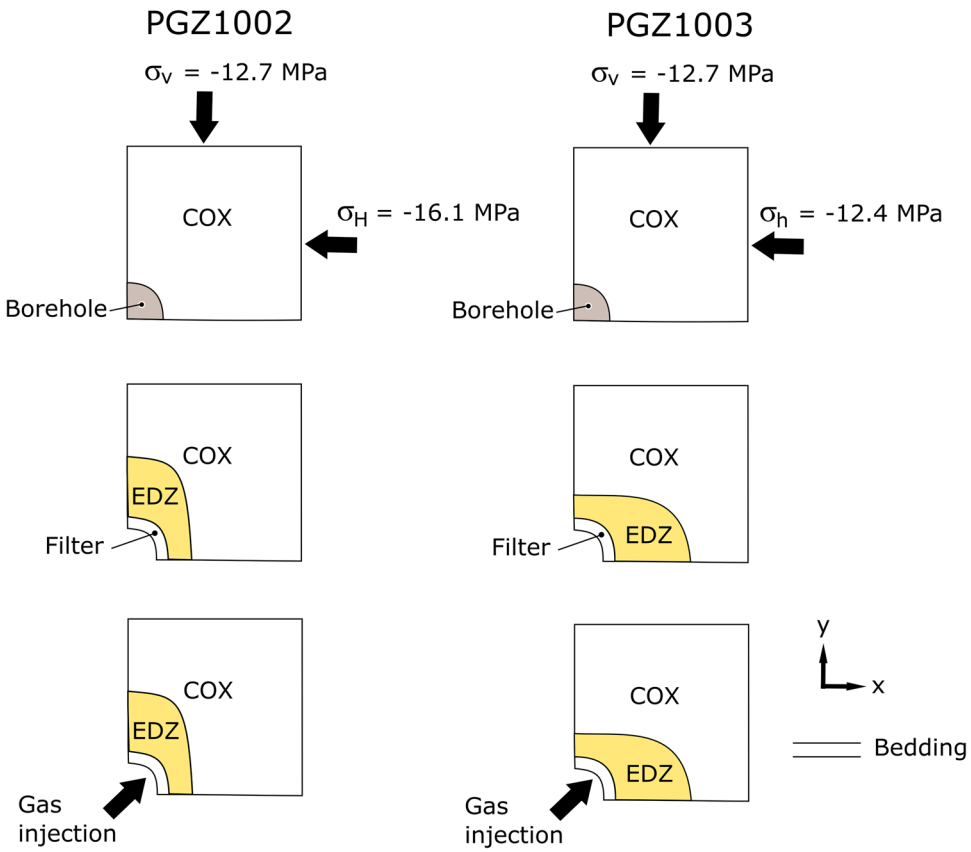

Fig. 3 Schematic drawing of the processes taking place for (PGZ1002) the borehole in the direction of the minor horizontal stress and (PGZ1003) the borehole in the direction of the major horizontal stress

claystone (de La Vaissière et al. 2014). The PGZ experiment started in 2009 with the experimental characterisation of hydraulically-induced fractures and the influence of the EDZ. Since 2020, a second phase of the experiment has been conducted, this time focusing on the effects of stress orientation on fracture development. The numerical calculation of the PGZ experiment is carried out in the framework of the current phase of the DECOVALEX project (DECOVALEX 2022). For the numerical simulations, the dimensions of the borehole, the gas-injection rate and most of the rock properties were provided by the DECOVALEX project.

Several boreholes were drilled in the GEX drift for the PGZ experiment (de La Vaissière et al. 2019). In the following, two of them are examined: one parallel to the minor horizontal stress (PGZ1002) and one parallel to the major horizontal stress (PGZ1003). The dimensions of the EDZ, created in the process of drilling can be estimated by in-situ investigations (Armand et al. 2014; de La Vaissière et al. 2015; Guayacán-Carrillo et al. 2015). The length of the borehole is 35 m and the radius of the borehole is $r_b = 0.038$ m. After the excavation process, a filter was inserted to which a Neumann boundary condition is attached to simulate the gas inflow. The inner radius of the filter is $r_i = 0.033$ m. A schematic representation of the processes taking place and the estimation of the dimension of the EDZ are shown in Fig. 3. This shows the drilling process and the following gas injection in three stages for both boreholes. PGZ1002 is drilled in parallel with the minor horizontal stress (σ_h) and PGZ1003 in parallel with the major horizontal stress (σ_H). Based on various in-situ investigations, the EDZ is expected to form as shown in the figure.

3.2 Model Parameter

The numerical model is based on the finite element method. The domain has a side length of 5 m. The 2D mesh has 3420 nodes and 3149 quadratic elements. At the beginning of the simulation, the COx claystone is fully saturated with a pore pressure of $p_p = 4.7$ MPa. The pore pressure is calculated from gas pressure and capillary pressure according to Eq. (5). Since the COx is fully saturated, the initial gas pressure is $p_g = 0.1$ MPa and the initial capillary pressure is $p_c = -4.7$ MPa. A Dirichlet condition with no displacement applies to all boundaries, except for the two boundaries where the stress is applied. Furthermore, on the far boundaries there are Dirichlet boundaries that keep the gas pressure at $p_g = 0$ Pa and the capillary pressure at $p_c = -4.7$ MPa. The initial conditions in the filter are determined by measurements during the experiment. A gas pressure of $p_g = 4.7$ MPa was built up and a saturation of approx. $S_w = 0.6$ was estimated, which corresponds to a capillary pressure of $p_c = 9.0$ kPa. Most of the rock and fluid parameter values

Table 2 Model parameter from DECOVALEX (2022) and Wang et al. (2021)

Model parameter	Symbol	COx	Filter	Unit
Biot coefficient	α	0.8	1.0	–
Cohesive strength	c	1.0	–	MPa
Density of solid grains	ρ_s	2770	1660	kg/m^3
Fitting parameter dilatancy-dependent permeability	b_1,b_2,b_3	4000, 400, 600	–	–
Fitting parameter failure index	b	3	–	–
Friction angle	φ	15	–	°
Gas entry pressure	p_{entry}	15	0.005	MPa
Intrinsic permeability	$\mathbf{k}$	$\|4 \cdot 10^{-20} \perp 1.3 \cdot 10^{-20}$	$1 \cdot 10^{-16}$	m^2
Maximum degree of saturation	S_{max}	1	1	–
Non-wetting dynamic viscosity	η_g	$1.79 \cdot 10^{-5}$		Pa s
Non-wetting phase density	ρ_g	Ideal gas law(0.162 at 1 atm)		kg/m^3
Non-wetting phase molar mass	$M^{N}{}_{2}$	0.028		kg/mol
Poisson ‘s ratio	$\boldsymbol{\nu}$	$\|0.3 \perp 0.2$	0.3	–
Porosity	ϕ	0.18	0.5	–
Reference permeability	k_r	$1 \cdot 10^{-19}$	–	m^2
Residual degree of saturation	S_{res}	0.05	0.05	–
Shear modulus	$\mathbf{G}$	$\|1.9 \perp 1.7$	–	GPa
Tensile strength	σ_t	3	–	MPa
Tortuosity	T	2	1	–
Van Genuchten parameter	n	1.49	1.6	–
Wetting-dynamic viscosity	η_w	$1.0 \cdot 10^{-3}$		Pa s
Wetting-phase density	ρ_w	$1.0 \cdot 10^{3}$(STP)		kg/m^3
Wetting-phase molar mass	$M^{H}{}_{2}{}^{O}$	0.018		kg/mol
Young’s modulus	$\mathbf{E}$	$\|6.0 \perp 4.0$	10	GPa

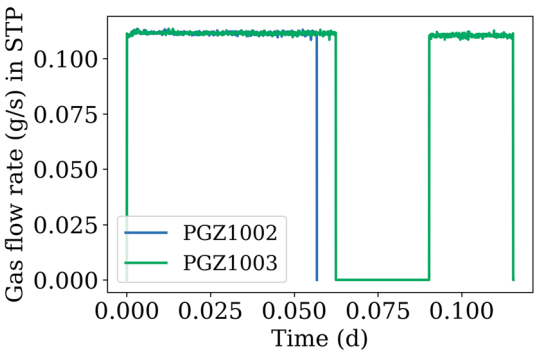

Fig. 4 Measured gas flow rate in the in-situ gas-injection test

were provided in the DECOVALEX project description and can be found in Table 2. The values for the failure-index permeability model and the Mohr–Coulomb failure criterion are from Wang et al. (2021) and are already calibrated to COx claystone.

During the gas-injection test, the gas flow rate was measured in standard temperature and pressure (STP). The presented gas flow rate was used in the in-situ experiments and are applied in the respective models (Fig. 4). The standard Galerkin finite element approach is applied for spatial discretisation of the domain. Linear shape functions are employed for gas pressure and capillary pressure, while quadratic shape functions are employed for the displacements. The time discretisation is carried out according to the implicit Euler method with a fixed time step size. The time increment varies between 60 s during the injection phase and 500 s during the decay phase. The set of equations is solved by a staggered scheme and linked with a coupling loop for each time step until convergence is reached. The biconjugate gradient stabilized method (BiCGSTAB) is used as a linear solver with an overall error tolerance of 10^{-16}. The Newton–Raphson iteration scheme is used as a nonlinear solver with a relative tolerance of 10^{-6}.

The parameter b_1, b_2 and b_3 of the dilatancy-dependent permeability model were calibrated so that the calculated gas pressure in the injection filter matches the measured gas pressure during the gas-injection test. The permeability model with failure index was applied as well, to achieve the closest possible similarity to the experimental gas injection test. Figure 5 shows the calibrated values and their effect in the H^{2}M coupling regarding the permeability.

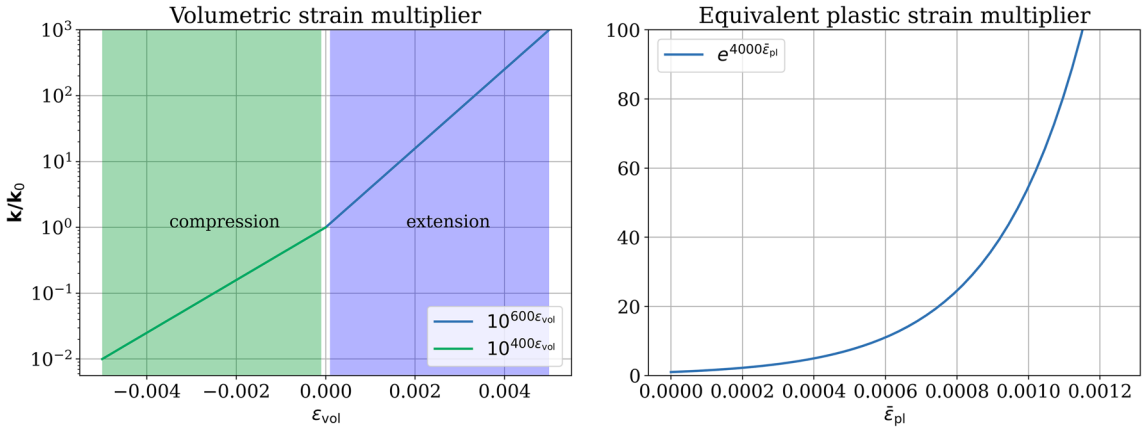

Fig. 5 Dilatancy-dependent permeability model with calibrated values

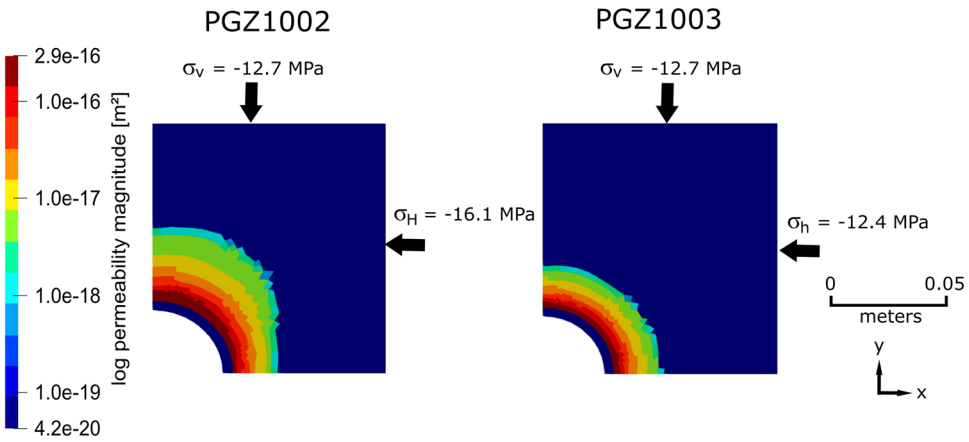

Fig. 6 Excavation-induced permeability in log-scale for PGZ1002 and PGZ1003

4 Results

4.1 Failure-Index Permeability for PGZ1002 and PGZ1003

The first step of the simulation is the excavation of the borehole. The failure-index permeability based on the Mohr–Coulomb model calculates the permeability around the borehole (Fig. 6). The calculated range of the EDZ is approximately 0.03–0.05 m into the claystone. This means that the calculation is within the range of measured dimensions of the EDZ in the vicinity of boreholes for COx (Armand et al. 2014). It can be observed that the influence of the stress distribution has a greater influence in the simulation on the formation of the EDZ than the transversal isotropic behaviour of the COx. The structure in the PGZ1002 model corresponds in shape to the measurements, schematically shown in Fig. 1. The calculated EDZ in the PGZ1003 model does not completely correspond in shape to the measurements. This is because in the failure-index model, the stress distribution is mainly responsible for the development of the EDZ, and the transversal isotropic behaviour of the COx has less influence. The calculated EDZ of borehole PGZ1002 extends approximately 0.05 m vertically and 0.025 m horizontally into the rock. Whereas the calculated EDZ of borehole PGZ1003 extends approximately 0.02 m vertically and only 0.03 m horizontally into the rock.

4.2 Dilatancy-Induced Gas Flow

To better analyze the influence of the respective constitutive models on permeability and pressures, base tests for both models and four model configurations (cases) are presented below:

Base test: PGZ1002 & 1003 without failure-index permeability without dilatancy-controlled permeability
Case A: PGZ1002 with failure-index permeability without dilatancy-controlled permeability

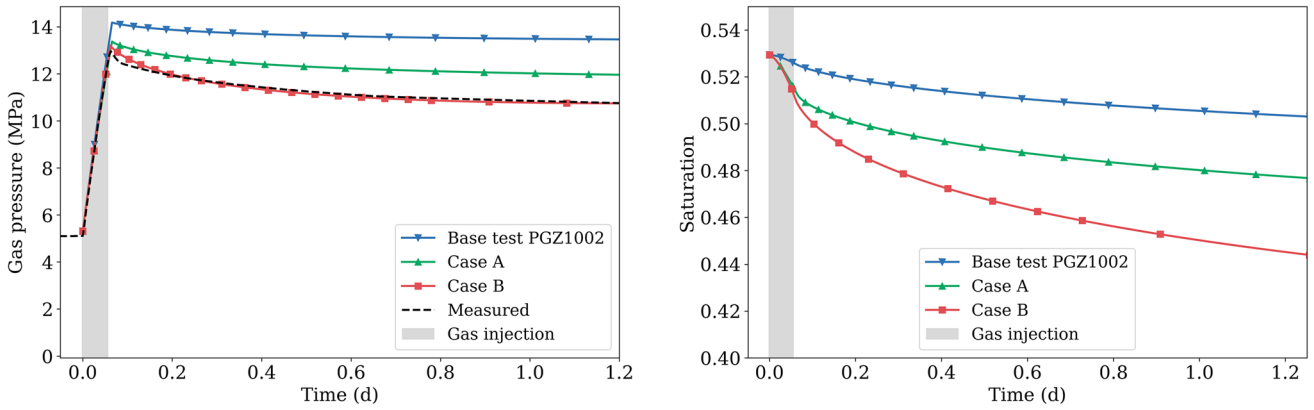

Fig. 7 Temporal evolution of gas pressure and water saturation during the injection and decay phase for PGZ1002. The section with gas injection are marked in grey

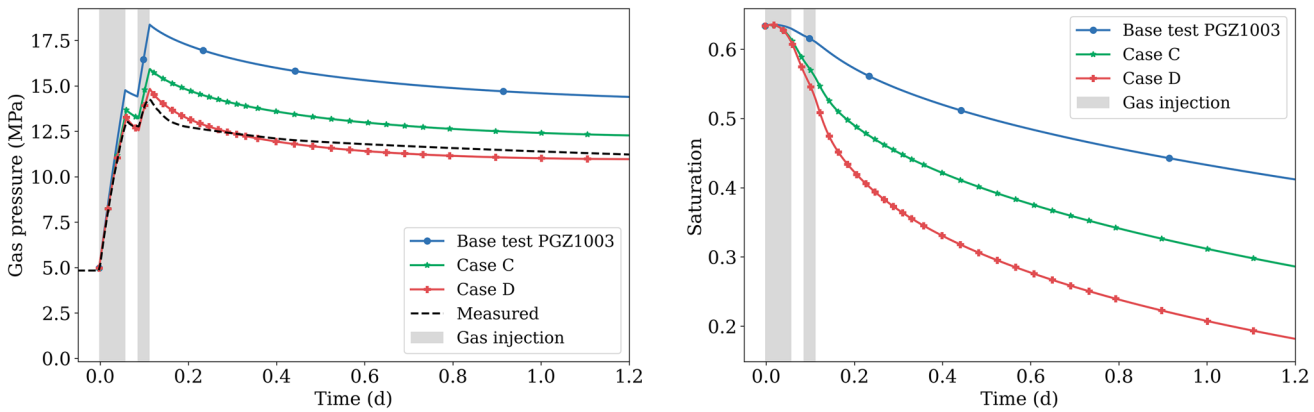

Fig. 8 Development of gas pressure and water saturation during the injection and decay phase for PGZ1003 the measured gas pressure. The sections with gas injection are marked in grey

Case B: PGZ1002 with failure-index permeability and dilatancy-controlled permeability
Case C: PGZ1003 with failure-index permeability without dilatancy-controlled permeability
Case D: PGZ1003 with failure-index permeability and dilatancy-controlled permeability

The validation of the approach and the comparison between the respective model cases is performed with the gas pressure and the water saturation in the filter. The measured values for the gas pressure in the filter are included as a black dashed line for comparison. The pressure and saturation development during gas injection and the decay phase of PGZ1002 is shown in Fig. 7 and for PGZ1003 in Fig. 8.

The figures show that the calculation without an additional constitutive equation (base test) describing the hydromechanical coupling misses the measured values by far. The gas pressure in the injection filter is overestimated by 1.5 MPa (PGZ1002) and 4 MPa (PGZ1003). By applying the failure-index permeability model, a better agreement with the measured gas pressure can be achieved. Only at very high pressures (above ~ 12 MPa) does an overestimation of the gas pressure of 1—2 MPa in the injection filter become apparent in the two models. The pressure corresponds approximately to the minimum principal stress (11.7 MPa) beyond which dilatant micro tensile cracks occur. The additional application of the dilatancy-dependent permeability model demonstrates that the maximum gas pressures in the filter can be better predicted with this additional constitutive model.

The increased gas pressure in the filter affects the liquid pressure near the borehole, since water is displaced from the injection filter into the COx. Figure 9 shows the fluid pressure for selected points near the borehole. The figure shows that the high liquid pressure quickly transfers from the injection filter into the COx and levels off after a few hours at close range. The effect is more obvious in case B and D where the dilatancy-controlled permeability model was also

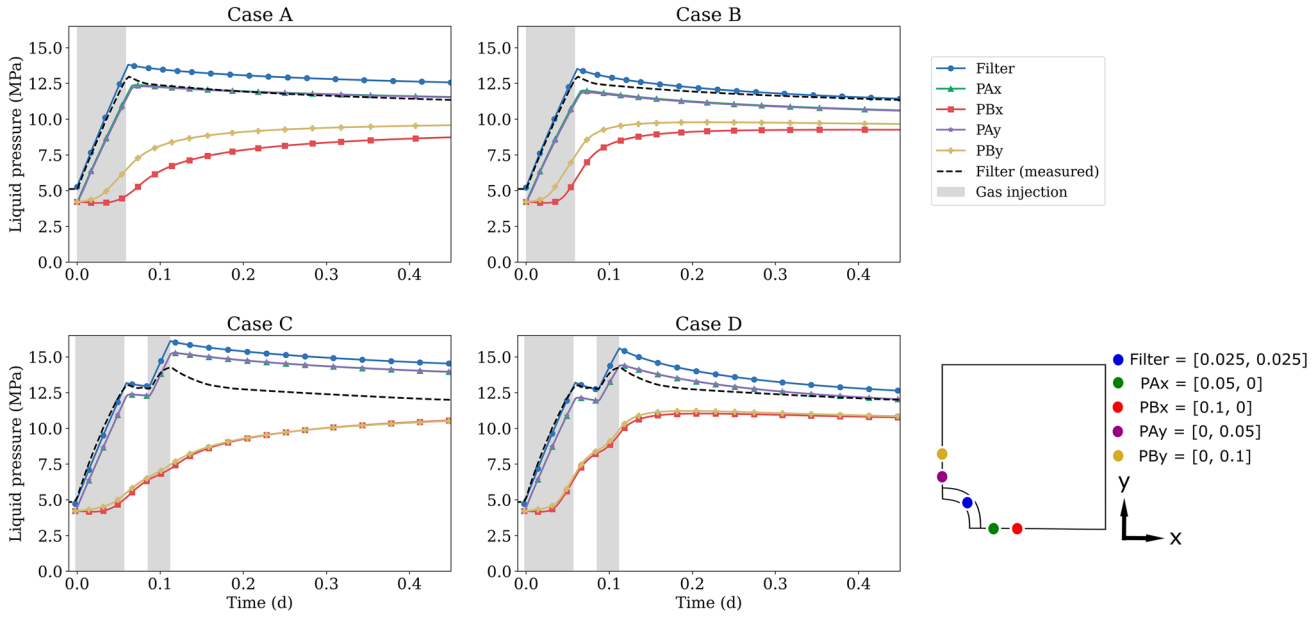

Fig. 9 Liquid pressure for all four cases at different points in the injection filter and COx. The measured liquid pressure in the filter is added for comparison. The sections with gas injection are marked in grey

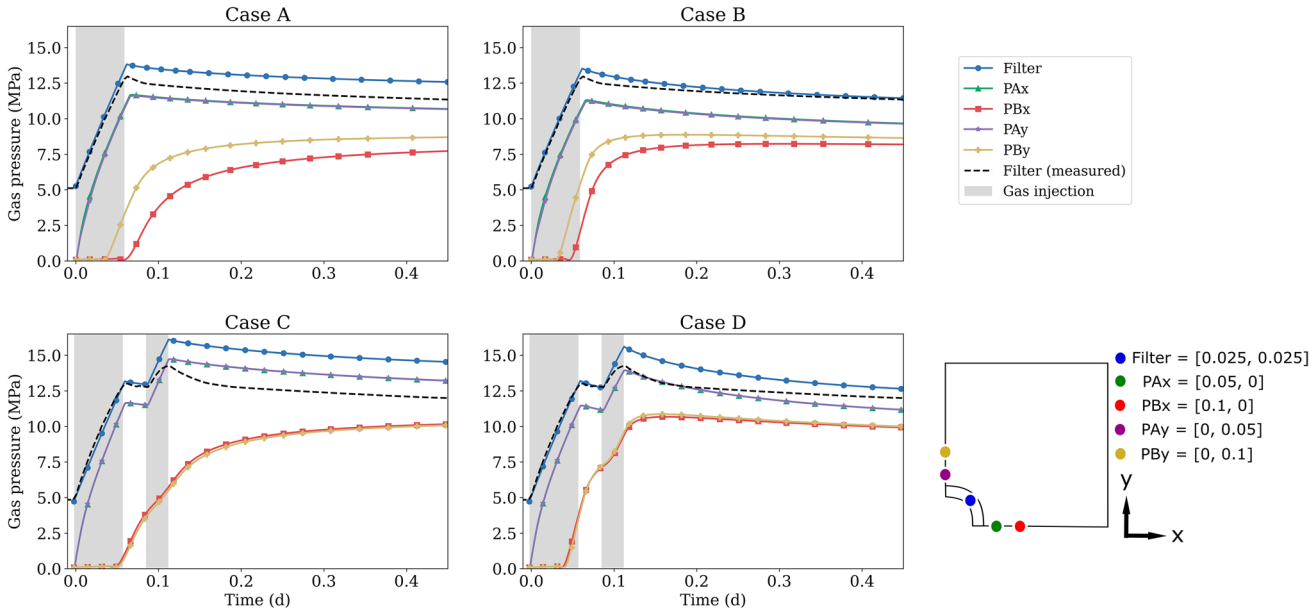

Fig. 10 Gas pressure for all four cases at different points in the injection filter and COx. The measured gas pressure in the filter is added for comparison. The sections with gas injection are marked in grey

used. The orthotropic behaviour of the COx is minimized in case C and D by the shape of the EDZ.

Figure 10 shows the gas pressure for selected points near the borehole. The gas pressure evolution is similar to the liquid pressure, but the increase is stronger and the gas pressure in the COx claystone is 0.1 MPa at the beginning of the calculation. This corresponds to the initial condition for the gas pressure, which was selected here according to the atmospheric pressure, since there is no gas phase in the claystone at the beginning of the calculation, since the claystone is fully saturated. It can also be observed that the calculation can be simulated better at lower pressures where a microfacture-induced gas flow at lower gas pressures occurs (PGZ1002) than at higher gas pressures (PGZ1003).

5 Conclusion

The approach to combine two independent constitutive models regarding the hydro-mechanically coupled processes during an excavation and gas-injection test was demonstrated on a number of models. The approach uses the dominant mechanical stress states of the analyzed processes to combine the sets of equations without creating a reciprocal coupling. Thus, only one permeability model is used at a time for a specific stress state and never both at the same time and stress state. The equation sets are thereby adjusted to the extent that they merge continuously into one another. To be precise, the transition occurs at compressive stress, namely when the yield strength is exceeded the index failure criterion formulates an increasing permeability, below the yield strength the compression leads to a decrease in permeability, simulated by the strain-dependent permeability model. The application was carried out in a well-studied area of the COx argillaceous rock formation. The drilling of two boreholes was simulated and subsequent gas-injection tests were calculated. The simulation was carried out in a coupled H^2M finite element model, calculated with the open-access software OGS. The evaluation of the hydraulic and mechanical parameters was conducted with measured data recorded during the gas-injection test for the PGZ experiment. The comparison with the measured data and between the test cases indicates the following:

- The failure-index permeability model has calculated plausible results regarding the extent and magnitude of the EDZ, which are also within the range of published data. However, when applying the Mohr–Coulomb flow criterion, the applied model cannot accurately reproduce the structure of the BDZ in the PGZ1003 model, which has an assumed ellipsoidal shape due to the transversely isotropic behavior of the COx.
- The combination of both constitutive equations can reflect the development of the gas pressure in the filter better than one equation alone could.
- The decay phases are well reproduced for the combined approach in cases B and D.

The developed approach has been successfully applied to the modelling of gas percolation in claystone and could prove to be a valuable tool for the safety analysis of a future nuclear waste repository.

Acknowledgements This research was conducted within the DECOVALEX-2023 project. DECOVALEX is an international research project comprising participants from industry, government, and academia, focusing on development of understanding, models and codes in complex coupled problems in sub-surface geological and engineering applications. DECOVALEX-2023 is the current phase of the project. The authors appreciate the DECOVALEX-2023 Funding Organisations ANDRA, BASE, BGE, BGR, CAS, CNSC, COVRA, US DOE, ENRESA, ENSI, JAEA, KAERI, NWMO, RWM, SÚRAO, SSM and Taipower for their financial and technical support of the work described in this paper. The statements made in the paper are, however, solely those of the authors and do not necessarily reflect those of the Funding Organisations. This work was further supported by the German Federal Ministry for Economic Affairs and Climate Action (BMWK).

Funding Open Access funding enabled and organized by Projekt DEAL. No funding was received for conducting this study.

Data availability The data that support the findings of this study are available from the corresponding author upon reasonable request.

Declarations

Conflict of interest The authors declare that they have no known competing financial interests or personal relationships that could have appeared to influence the work reported in this paper.

References

Amri A, Saâdi Z, Ababou R (2022) Parametric sensitivity to capillary entry pressure in two-phase water-gas flow models: deep geologic disposal of radioactive waste. Transp Porous Media 145(1):13–43. https://doi.org/10.1007/s11242-022-01780-w

Armand G, Leveau F, Nussbaum C, de La Vaissiere R, Noiret A, Jaeggi D, Landrein P, Righini C (2013) Geometry and properties of the excavation-induced fractures at the Meuse/Haute-Marne URL Drifts. Rock Mech Rock Eng 47(1):21–41. https://doi.org/10.1007/s00603-012-0339-6

Armand G, Leveau F, Nussbaum C, de La Vaissiere R, Noiret A, Jaeggi D, Landrein P, Righini C (2014) Geometry and properties of the excavation-induced fractures at the Meuse/Haute-Marne URL drifts. Rock Mech Rock Eng 47(1):21–41. https://doi.org/10.1007/s00603-012-0339-6

Belmokhtar M, Delage P, Ghabezloo S, Tang A-M, Menaceur H, Conil N (2016) Poroelasticity of the Callovo-Oxfordian claystone. Rock Mech Rock Eng 50(4):871–889. https://doi.org/10.1007/s00603-016-1137-3

Birkholzer JT, Bond AE (2022) DECOVALEX-2019: An international collaboration for advancing the understanding and modeling of coupled thermo-hydro-mechanical-chemical (THMC) processes in geological systems. Int J Rock Mech Min Sci. https://doi.org/10.1016/j.ijrmms.2022.105097

Braun P, Ghabezloo S, Delage P, Sulem J, Conil N (2020) Transversely isotropic poroelastic behaviour of the Callovo-Oxfordian CLAYSTONE: a set of stress-dependent parameters. Rock Mech Rock Eng 54(1):377–396. https://doi.org/10.1007/s00603-020-02268-z

Chiarelli AS, Shao JF, Hoteit N (2003) Modeling of elastoplastic damage behavior of a claystone. Int J Plast 19(1):23–45. https://doi.org/10.1016/S0749-6419(01)00017-1

Darcy H (1856) Les fontaines publiques de la ville de Dijon: exposition et application. Victor Dalmont, Paris, pp 305–310

De La Vaissière R, Gerard P, Radu J-P, Charlier R, Collin F, Granet S, Talandier J, Piedevache M, Helmlinger B (2014) Gas injection test in the Callovo-Oxfordian claystone: data analysis and numerical modelling. Geol Soc Spec Publ 400(1):427–441. https://doi.org/10.1144/sp400.10

de La Vaissière R, Armand G, Talandier J (2015) Gas and water flow in an excavation-induced fracture network around an underground drift: a case study for a radioactive waste repository in clay rock. J Hydrol 521:141–156. https://doi.org/10.1016/j.jhydrol.2014.11.067

de La Vaissière R, Talandier J, Armand G, Vu M-N, Cornet FH (2019) From Two-Phase Flow to Gas Fracturing into Callovo-Oxfordian Claystone. 53rd U.S. Rock Mechanics/Geomechanics Symposium, New York

DECOVALEX. (2022). Task A. https://decovalex.org/D-2023/task-a.html. Accessed 11 Nov 2022.

Delay J, Conil N, de La Vaissière R (2011) Meuse/Haute-Marne underground research center – Technologies and techniques for studying gas flow and thermal properties of an indurated clay-rock. i-DUST. https://doi.org/10.1051/idust/201103001

Gerard P, Harrington J, Charlier R, Collin F (2014) Modelling of localised gas preferential pathways in claystone. Int J Rock Mech Min Sci 67:104–114. https://doi.org/10.1016/j.ijrmms.2014.01.009

Guayacán-Carrillo L-M, Sulem J, Seyedi DM, Ghabezloo S, Noiret A, Armand G (2015) Analysis of long-term anisotropic convergence in drifts excavated in Callovo-Oxfordian claystone. Rock Mech Rock Eng 49(1):97–114. https://doi.org/10.1007/s00603-015-0737-7

Horseman ST. (1996). Generation and migration of repository gases: some key considerations Int. Two-day Conf. on Radioaktive Waste Disposal, London.

Jung S, Vu MN, Ghabezloo S, Pouya A (2023) Effect of anisotropic creep on the convergence of deep drifts in Callovo-Oxfordian claystone. IOP Conf Ser Earth Environ Sci. https://doi.org/10.1088/1755-1315/1124/1/012046

Kolditz O, Bauer S, Bilke L, Böttcher N, Delfs JO, Fischer T, Görke UJ, Kalbacher T, Kosakowski G, McDermott CI, Park CH, Radu F, Rink K, Shao H, Shao HB, Sun F, Sun YY, Singh AK, Taron J, Walther M, Wang W, Watanabe N, Wu Y, Xie M, Xu W, Zehner B (2012) OpenGeoSys: an open-source initiative for numerical simulation of thermo-hydro-mechanical/chemical (THM/C) processes in porous media. Environ Earth Sci 67(2):589–599. https://doi.org/10.1007/s12665-012-1546-x

Labuz JF, Zang A (2012) Mohr-coulomb failure criterion. Rock Mech Rock Eng 45(6):975–979. https://doi.org/10.1007/s00603-012-0281-7

Le AD, Nguyen TS (2015) Hydromechanical response of a bedded argillaceous rock formation to excavation and water injection. Can Geotech J 52(1):1–17. https://doi.org/10.1139/cgj-2013-0324

Mánica M, Gens A, Vaunat J, Ruiz DF (2017) A time-dependent anisotropic model for argillaceous rocks. Application to an underground excavation in Callovo-Oxfordian claystone. Comput Geotech 85:341–350. https://doi.org/10.1016/j.compgeo.2016.11.004

Mualem Y (1976) A new model for predicting the hydraulic conductivity of unsaturated porous media. Water Resour Res 12(3):513–522

Nagel T, Minkley W, Böttcher N, Naumov D, Görke U-J, Kolditz O (2017) Implicit numerical integration and consistent linearization of inelastic constitutive models of rock salt. Comput Geotech 182:87–103. https://doi.org/10.1016/j.compstruc.2016.11.010

Olivella S, Alonso EE (2008) Gas flow through clay barriers. Geotechnique 58(3):157–176. https://doi.org/10.1680/geot.2008.58.3.157

Pardoen B, Collin F (2017) Modelling the influence of strain localisation and viscosity on the behaviour of underground drifts drilled in claystone. Comput Geotech 85:351–367. https://doi.org/10.1016/j.compgeo.2016.05.017

Plúa C, Vu MN, Armand G, Rutqvist J, Birkholzer J, Xu H, Guo R, Thatcher KE, Bond AE, Wang W, Nagel T, Shao H, Kolditz O (2021) A reliable numerical analysis for large-scale modelling of a high-level radioactive waste repository in the Callovo-Oxfordian claystone. Int J Rock Mech Min Sci. https://doi.org/10.1016/j.ijrmms.2020.104574

Radeisen E, Shao H, Hesser J, Kolditz O, Xu W, Wang W (2023a) Simulation of dilatancy-controlled gas migration processes in saturated bentonite using a coupled multiphase flow and elasto-plastic H2M model. J Rock Mech Geotech Eng 15(4):803–813. https://doi.org/10.1016/j.jrmge.2022.05.011

Radeisen E, Shao H, Hesser J, Naumov D, Wang W, Kolditz O (2024) Modelling of preferential gas flow in saturated bentonite using a bimodal strain-dependent pore model Appl Clay Sci 249. https://doi.org/10.1016/j.clay.2023.107232

Radeisen E, Shao H, Pitz M, Hesser J, Wang W (2023b) Derivation of heterogeneous material distributions and their sensitivity to HM-coupled two-phase flow models exemplified with the LASGIT experiment. Abstr Environ Earth Sci 82(14). https://doi.org/10.1007/s12665-023-11004-z

Senger R, Romero E, Ferrari A, Marschall P (2014) Characterization of gas flow through low-permeability claystone: laboratory experiments and two-phase flow analyses. Geol Soc Spec Publ 400(1):531–543. https://doi.org/10.1144/sp400.15

Senger R, Romero E, Marschall P (2018) Modeling of gas migration through low-permeability clay rock using information on pressure and deformation from fast air injection tests. Transp Porous Media 123(3):563–579. https://doi.org/10.1007/s11242-017-0962-5

Seyedi DM, Armand G, Noiret A (2017) "Transverse Action"—A model benchmark exercise for numerical analysis of the Callovo-Oxfordian claystone hydromechanical response to excavation operations. Comput Geotech 85:287–305. https://doi.org/10.1016/j.compgeo.2016.08.008

Seyedi DM, Plúa C, Vitel M, Armand G, Rutqvist J, Birkholzer J, Xu H, Guo R, Thatcher KE, Bond AE, Wang W, Nagel T, Shao H, Kolditz O (2021) Upscaling THM modeling from small-scale to full-scale in-situ experiments in the Callovo-Oxfordian claystone. Int J Rock Mech Min Sci. https://doi.org/10.1016/j.ijrmms.2020.104582

Souley M, Armand G, Kazmierczak JB (2017) Hydro-elasto-viscoplastic modeling of a drift at the Meuse/Haute-Marne underground research laboratoratory (URL). Comput Geotech 85:306–320. https://doi.org/10.1016/j.compgeo.2016.12.012

van Genuchten MT (1980) A closed-form equation for predicting the hydraulic conductivity of unsaturated soils. Soil Sci Soc Am J 44(5):892–898. https://doi.org/10.2136/sssaj1980.03615995004400050002x

Vu M-N, Guayacán Carrillo LM, Armand G (2020) Excavation induced over pore pressure around drifts in the Callovo-Oxfordian claystone. Eur J Environ Civ Eng. https://doi.org/10.1080/19648189.2020.1784800

Wang W, Rutqvist J, Görke U-J, Birkholzer J., Kolditz O (2011) Non-isothermal flow in low permeable porous media: a comparison of Richards' and two-phase flow approaches. Environ Earth Sci 62(6):1197–1207. https://doi.org/10.1007/s12665-010-0608-1

Wang W, Shao H, Nagel T, Kolditz O (2021) Analysis of coupled thermal-hydro-mechanical processes during small scale in situ heater experiment in Callovo-Oxfordian clay rock introducing a failure-index permeability model. Int J Rock Mech Min Sci. https://doi.org/10.1016/j.ijrmms.2021.104683

Xu WJ, Shao H, Hesser J, Wang W, Schuster K, Kolditz O (2013) Coupled multiphase flow and elasto-plastic modelling of in-situ gas injection

experiments in saturated claystone (Mont Terri Rock Laboratory). Eng Geol 157:55–68. https://doi.org/10.1016/j.enggeo.2013.02.005

Yang J, Fall M, Guo G (2020) A three-dimensional hydro-mechanical model for simulation of dilatancy controlled gas flow in anisotropic claystone. Rock Mech Rock Eng 53(9):4091–4116. https://doi.org/10.1007/s00603-020-02152-w

Zhang C, Rothfuchs T (2004) Experimental study of the hydro-mechanical behaviour of the Callovo-Oxfordian argillite. Appl Clay Sci 26(1–4):325–336. https://doi.org/10.1016/j.clay.2003.12.025